The International Journal of Advanced Manufacturing Technology (2023) 129:3047–3062
https://doi.org/10.1007/s00170-023-12384-z

ORIGINAL ARTICLE

# Convolutional neural networks for melt depth prediction and visualization in laser powder bed fusion

Francis Ogoke[1] · William Lee[1] · Ning-Yu Kao[2] · Alexander Myers[1] · Jack Beuth[1] · Jonathan Malen[1] · Amir Barati Farimani[1,2,3]

Received: 17 February 2023 / Accepted: 22 September 2023 / Published online: 21 October 2023


**Abstract**
Powder bed fusion is a method of additive manufacturing (AM) where parts are constructed by iteratively melting metal cross-sections to build complex 3D structures. Defects often form during the printing process, where the dynamics of the melt pool can directly contribute to the formation of porous defects in the final part. For instance, insufficient overlap of the produced melt pools can result in unmelted regions of powder, while deep, unstable vapor depression cavities can lead to spherical voids becoming trapped in the substrate. Therefore, in situ of monitoring the melt pool during the melting process can telegraph the formation of defects and assist the creation of fully dense parts. Here, we augment data-driven-based monitoring techniques to enable the 3D visualization of the melt pool underneath the surface, based on the melt pool surface temperature and processing parameters. Specifically, a convolutional neural network (CNN) predicts the topography of the melt pool and keyhole cavity, based on the surface temperature data near the laser focal point and the nominal operating conditions. The data for the laser powder bed fusion process used to train the model is produced by full-field simulations of the meso-scale melting process, with the CFD software FLOW-3D. Data augmentation techniques are implemented to ensure generalizable performance in cases where the temperature data may be obscured and to ensure sharp, accurate predictions of the melt pool boundaries.

**Keywords** Additive manufacturing · Laser powder bed fusion · Convolutional neural networks · Deep learning

## 1 Introduction

Laser powder bed fusion (L-PBF) is an emerging technology within additive manufacturing (AM), enabling the construction of parts with complex geometries. During L-PBF, a heat source is used to melt and fuse successive layers of metallic powder. This process allows the user to fabricate parts that would be difficult to manufacture with conventional methods and also allows for rapid prototyping [1, 2].

One challenge preventing wider L-PBF adoption in high-precision applications is the tendency for defects and residual stresses to form during the melting process [3]. The melt pool, formed by the instantaneous interaction of the laser with the substrate, is a crucial determinant of the microstructural features, stress distributions, and defect formation in the printed part. Thus, dynamics of the melt pool and the properties of the resulting porosity distribution have been closely studied to establish relationships to the properties of the manufactured component [4–7]. Additionally, during high energy density melting, the substrate will vaporize and exert pressure on the melt pool free surface, creating a vapor cavity known as a keyhole. If this keyhole is unstable, the vapor cavity can potentially collapse and trap gas bubbles in the solidified product [8, 9]. Another defect that can occur is lack-of-fusion, which occurs when the successive layers of melt pools do not completely overlap, causing voids of unmelted powder to remain in the final component [9, 10].

To mitigate the occurrences of these defects, several methods for in situ monitoring of the melt pool have been proposed [11–13]. For instance, X-ray synchrotron imaging allows the user to visualize the melt pool cross-section with time scale resolutions on the order of nanoseconds [14]. During X-ray synchrotron imaging, the L-PBF process is recreated within the path of an X-ray incident beam, which enables the user

Francis Ogoke and William Lee contributed equally to this work.

✉ Amir Barati Farimani
barati@cmu.edu

Extended author information available on the last page of the article

to examine melt pool depth and keyhole morphology during the build process [8, 15, 16]. However, these methods may require extensive modifications to existing machinery to accommodate the X-ray technology [17]. Thermal cameras have also been implemented to find the temperature of the material on the powder bed, where large deviations in the temperature field could indicate that a defect has formed [18, 19]. For instance, specialized high-resolution cameras, such as recoater-based line cameras, can be used to physically observe defects that are forming as the part is being made [20]. These differing monitoring methods can be combined to provide multimodal streams of information about the melt pool dynamics [21].

These monitoring methods have enabled large amounts of data from the melting process to be collected on an ongoing basis. Therefore, data-driven methods can be leveraged to discover relationships in the collected monitoring data and automatically discover correlations between the observed properties of the build and the probability of defect formation [22–24]. For instance, Gobert et al. successfully performed in situ detection of lack-of-fusion pores by extracting the geometrical features of identified irregularities in the build image [25]. These geometrical features were used to identify areas of the build plate likely to form defects, using an ensemble of support vector machine models. In cases where manual feature extraction may not be feasible, deep learning methods have demonstrated promise in automatically detecting relevant features directly from image data [18, 20, 26]. One common deep learning model for processing sensor and image information is the convolutional neural network (CNN), which automatically extracts spatial structure in the data based on its relevance to the prediction target. To do so, a CNN learns the patterns within an image via convolutional filters and assigns weights depending on their importance [27]. In [28], Snow et al. (2021) predicted the presence of defects using data collected from in situ monitoring with CNNs, demonstrating improved generalization capabilities when presented with new build configurations not present in the training set.

With this work, we seek to predict the three-dimensional structure of the keyhole and melt pool, which have both been shown to have significant impact towards the mechanical performance of the manufactured component [9]. For instance, Cunningham et al. (2017) show that the stability of the keyhole cavity geometry can directly indicate whether pores will form in the finished part [8]. In related work, Tang et al. (2017) demonstrated that failures of the melt pool to overlap in three dimensions can lead to pockets of unmelted powder that result in porosity [10]. In this work, we predict the three-dimensional topology of the melt pool and keyhole cavity to generate a visualization of the current state of the melt pool. By parameterizing these quantities as 2D contour maps, we bypass the computational expense of training and predicting in a three-dimensional context, enabling the user to estimate the morphology of the melt pool below the surface in an on-going manner with a lightweight 2D model (Fig. 1). To simulate the obscuring of the camera by vapor and ejected spatter, the model is jointly trained on corrupted images via data augmentation techniques to avoid overfitting and improve generalization. Finally, the trained model is deployed on experimental thermal images to examine its extensibility to in situ monitoring contexts.

## 2 Methods

### 2.1 Simulation details

The simulation data for this work was generated by simulating 46 bare plate, single track simulations of Ti-6Al-4V at varying laser scan speed and power settings. The simulation duration is $500\mu s$, and snapshots of the melt pool are recorded at 5 $\mu s$ intervals for training the model. The FLOW-3D v11.2 CFD package is used to solve the governing equations describing the mass, momentum, and energy transfer present with a volume of fluid (VOF) model [29]. These equations are reproduced below:

$$\nabla \cdot (\rho \vec{v}) = 0 \tag{1}$$

$$\frac{\partial \vec{v}}{\partial t} + (\vec{v} \cdot \nabla)\vec{v} = -\frac{1}{\rho}\nabla \vec{P} + \mu \nabla^2 \vec{v} + \vec{g}(1 - \alpha(T - T_m)) \tag{2}$$

$$\frac{\partial h}{\partial t} + (\vec{v} \cdot \nabla)\, h = \frac{1}{\rho}\,(\nabla \cdot k \nabla T) \tag{3}$$

where $\vec{g}$ is gravity, $\alpha$ is the coefficient of thermal expansion, $\vec{P}$ is pressure, $\rho$ is the density, $\vec{v}$ is velocity, $h$ is the specific enthalpy, and $k$ represents heat conductivity. The intrinsic thermal parameters, $k$, $\rho$, and $C_p$, are temperature-dependent, with their behavior referenced from [30] for Ti-6Al-4V. The variation of density with temperature is modeled with the Boussinesq approximation [31].

The VOF method is used to define the fluid configuration [32] and simulate the free surface of the material. The conservation equation for the fluid volume fraction is referenced in Eq. 4. $F$ represents the fraction of the mesh cell volume occupied by fluid. When $F = 0$, the cell is considered a void region, representing the gas phase. To reduce the computational complexity of the model, the gas dynamics in

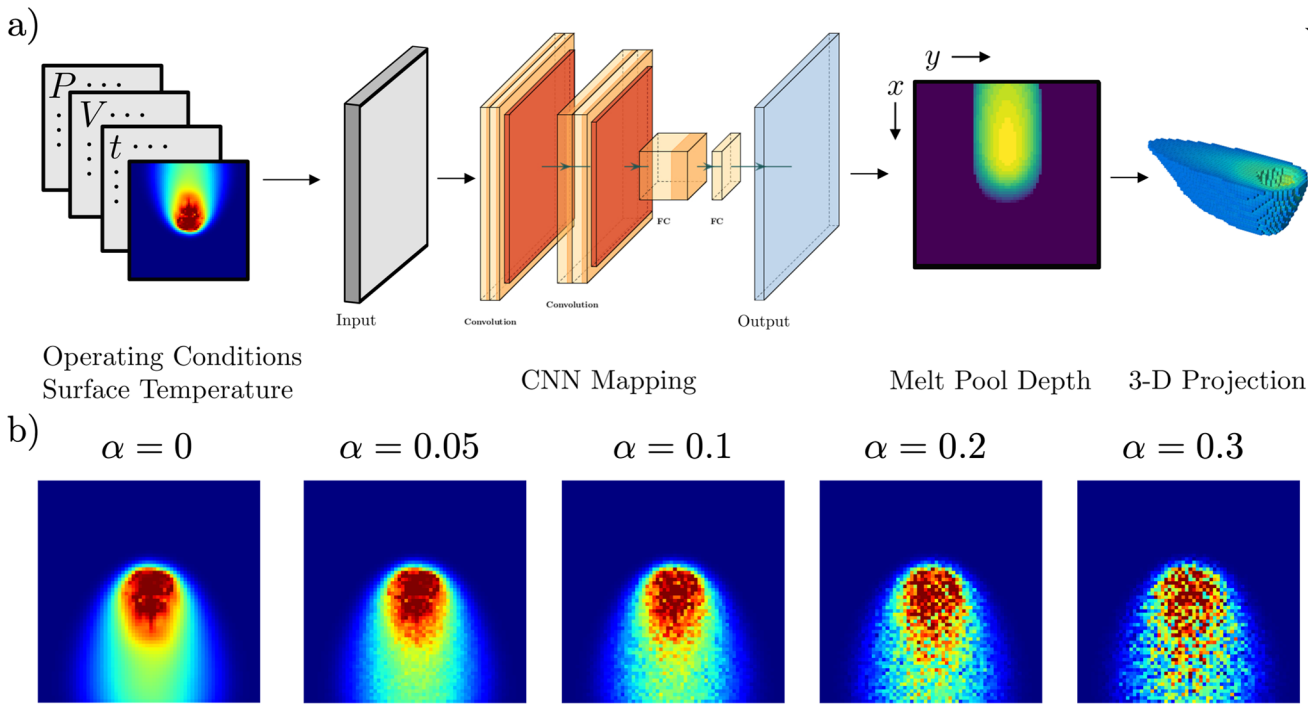


**Fig. 1** **a** In this model, a convolutional neural network (CNN) is used to map the local surface temperature created to the 3D projection of the resulting melt pool. The processing conditions (power, velocity) are combined with the surface temperature (time) and subsequently used to predict the melt pool depth, $D(x, y)$, at each point on the surface. This topology map can then be used to reconstruct a realization of the produced melt pool. **b** Random transformations are applied to increase the dataset size, including rotation and noise addition. The amount of noise added is parameterized by the constant $\alpha$

this region are not explicitly simulated. Instead, the pressure that the gas exerts on the free surface is approximated as a replacement of the gas dynamics.

$$\frac{\partial F}{\partial t} + (\nabla F \cdot v) = 0 \tag{4}$$

The laser beam is defined by a Gaussian distribution, parameterized by the laser power, $P$, and the laser beam radius, $r_0$.

$$q = \frac{P}{r_0^2 \pi} \exp\left\{-\left(\frac{\sqrt{2}r}{r_0}\right)^2\right\} \tag{5}$$

The top layer of surface cells is irradiated during simulation, and the corresponding heat flux propagates through the domain through conduction and convection mechanisms.

During the melting process, the evaporation of metal vapor can cause a keyhole-shaped vapor cavity to form in the melt pool. This cavity increases the effective absorptivity of the laser interaction with the melt pool due to reflection effects inside the cavity [33]. To model this behavior, the dependence of the absorptivity on the processing conditions is determined based on a scaling relationship introduced in [34].

This scaling relationship (Eq. 6) determines the absorptivity, $A$ as a function of the thermal diffusivity, $D$, beam radius, $r_0$, melting enthalpy $H_m$, and the processing parameters. As the heat input of the laser increases, the effects of multiple reflection due to the keyhole are intensified, and the absorptivity increases.

$$A = \left(0.70(1 - e^{-0.66y})\right) \tag{6}$$

$$y = \left(\frac{A_m P D}{\pi v H_m r_0^2 \sqrt{D r_0^2 / v}} (r_0 \sqrt{D r_0 / v})\right) \tag{7}$$

The evaporation mechanisms are simulated to model the influence of the vapor recoil pressure during the melting process. The recoil pressure is given by

$$P_s = a P_V \exp\left\{\frac{\Delta H_v}{(\gamma - 1) c_v T_v}\left(1 - \frac{T_v}{T}\right)\right\} \tag{8}$$

In the above equation, $\Delta H_v$ represents the heat of vaporization, and $a$ represents the ratio of energy exchange between phases as a fraction of the maximum energy exchange possible. Additionally, $\gamma$ represents the ratio of the

constant pressure and constant temperature specific heats, $C_v^{vap}$ is the constant volume heat capacity of the vapor, and $P_V$ and $T_V$ are the saturation temperature and pressure, respectively. The mass loss, $\dot{M}$, due to this evaporation process is modeled by the equation below.

$$\dot{M} = a\sqrt{\frac{1}{2\pi R\bar{T}}}(P_l^{sat} - P_p) \tag{9}$$

Here, $\bar{T}$ is the average temperature of the liquid along the free surface, $R$ is the gas constant, and $P_p$ is the partial pressure of the metal vapor.

This simulation is solved on a structured Cartesian mesh, with mesh elements of size 5 $\mu m$. A complete list of the values for material parameters used to simulate the melt pool behavior can be found in the Appendix, in Table 2.

To generate the surface temperature for a given timestep of the simulation, the 3D morphology of the surface is projected to a 2D image. A sample snapshot of the 3D simulation domain is shown in Fig. 2. First, disconnected particles ejected from the melt pool are removed from the domain. Then, the temperature of the point closest to the top surface for each vector, $T(x_i, y_j, \mathbf{z})$, is selected to be the corresponding point in the surface temperature image, $T_{surf}(x_i, y_j)$. The melt depth contour $d$ is generated in a similar manner, storing for each point, $d(x_i, y_j)$, the corresponding depth of the melt pool. These surface temperatures and depth contours were defined in a 64 × 64 pixel image, cropped, and centered on the location of the center of the laser at time $t$. Each image contains information for a 320$\mu m$ by 320$\mu m$ area around the center of the laser beam.

## 2.2 Data augmentation

Due to the computational expense of simulating powder bed fusion, data augmentation techniques were used to increase the size of the dataset. Two types of image augmentation are used to expand the dataset: arbitrary rotations of the surface temperature map and the addition of a scaled random noise image to the surface temperature. These rotation transformations are applied to allow the network to capture the melt pool depth as the laser travels in different directions. Noise additions to the input simulate measurement difficulties due to a physical camera. For the rotation augmentation, the original temperature map and the depth field are both rotated in 90 degree increments, such that the dataset consists of 0, 90, 180, and 270 degree rotations from the original image. The noise augmentation is performed by adding speckled Gaussian noise to the temperature field. This process is described in Eq. 10, where $\alpha$ refers to the strength of the noise relative to the signal and $\theta \sim N(0, 1)$ is a noise image sampled from the standard normal distribution. Examples of these augmentations can be seen in Fig. 1b.

$$T_{aug} = T + \alpha\theta T \tag{10}$$

After implementing these augmentations, the size of the training set was increased by a factor of five. This process reduces overfitting by increasing the amount of data available to the model and allowing the model to be generalizable in cases where experimental measurement difficulties can obscure the temperature data.

## 2.3 Model architecture

The CNN model used for this work was created using the PyTorch auto-differentiation library [35]. A CNN is a type of neural network that is most commonly used for image processing and can generally be applied in cases where input data is defined on a regularly spaced Cartesian grid [27]. The CNN model applies iterative convolution operations on the image in order to extract the features of the image most relevant to the prediction target. In this case, once those features are learned, these are fed into a dense neural network which predicts the flattened image for the depth of the melt pool. The pipeline of the model to predict the melt pool can be seen in Fig. 1a. An important feature of CNN models is that they are translation invariant, allowing the model to make accurate predictions even when the subject of the image is displaced relative to its original position.

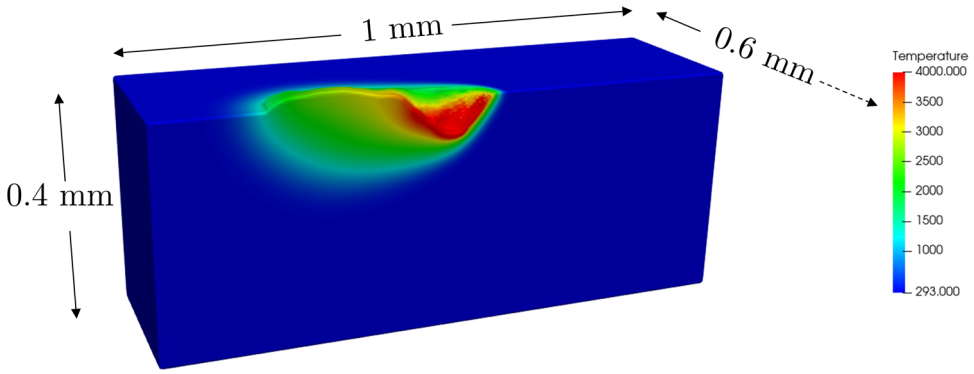


**Fig. 2** The temperature field during the laser powder bed fusion process, as simulated by FLOW-3D. In this instance, the laser power is 220 W, the laser scan speed is 1100 mm/s, and the substrate is Ti-6Al-4V. This simulation is performed with a constant mesh element size of 5$\mu m$

The hyperparameters defining the architecture of the model dictate the performance and convergence properties of the training process. Therefore, a Bayesian optimization-based process was used to automatically find the optimal configuration for the CNN model. During the hyperparameter optimization process, the kernel size and the channel size of each layer of the model were tuned in order to find the model with the lowest error on the validation dataset, using the Python package HyperOpt [36].

In order to increase the ability of the model to correctly predict the edges of the melt pool, a loss function based on a binary, thresholded image of the melt pool was implemented during training. This loss function modification was implemented to apply penalization to cases where melting was predicted in a zone that was not melted in the ground truth sample. Implementing this additional term to the loss function improves the model's ability to correctly predict the boundary contour of the melt pool and minimize noise. The following custom loss function was introduced to improve the prediction of the melt depth.

$$L(y_{true}, y_{pred}) = \begin{cases} (y_{pred} - y_{true})^2, & y_{true} \neq 0 \\ C * (y_{pred} - y_{true})^2, & y_{true} = 0. \end{cases} \quad (11)$$

## 3 Results and discussion

### 3.1 Model configuration

The CNN architecture consists of two blocks of convolution operations, followed by two fully connected dense layers. The two convolutional blocks are configured as a convolutional layer followed by a max pooling layer and a dropout step to reduce overfitting. Both convolutional blocks create a feature map of 128 channels, with a learned filter of size 5×5. Following the two convolutional layers, the final output is flattened and fed through two dense layers, with size 4608 and 2048, respectively, to produce the melt pool depth image. For each layer, the ReLU activation function was used. The value of $C$, 4.0, was chosen by selecting the value that minimized the difference between the predicted surface area and the ground truth surface area on the validation dataset. The ADAM optimizer was used to trained the model for 1000 epochs with a batch size of 70. Additionally, the training set is augmented to be five times the size of the original dataset by applying rotations and noise additions, as seen in Fig. 1b.

Five-fold cross validation was used to evaluate model performance. During this process, the dataset and labels are split into five folds, where the model is trained on four folds, and one fold is reserved to be used as a testing set. This process is repeated five times, such that each fold is used once as a testing set. Through cross validation, the mean absolute error (MAE) of the melt depth prediction task is 2.390 ± 0.925 $\mu$m, while the MAE with a conventional mean squared error loss function was 2.776 ± 0.756 $\mu$m. This demonstrates that the implemented loss function yields smaller error values by emphasizing the importance of the correct prediction of the melt pool boundaries. Similarly, the MAE on the keyhole depth prediction task was found to be 0.761 ± 0.15 microns for the validation dataset.

In order to assess the prediction performance of the model, we compare the predicted melt pool depths to the ground truth melt pool depths. This comparison is taken at different power and velocity combinations to examine how performance may change for different melt pool morphologies. Based on the images shown in Fig. 3, which describe the 2D topology images and the cross-section profile in a moving reference frame centered on the laser, the model is able to closely recreate the topology of the melt pool in the ground truth. In this figure, the isotherm of the temperature distribution at the melting temperature is also overlaid in black to allow for an easier qualitative comparison between the ground truth and predicted topology. This isotherm line is also used to ensure that the melt pool boundaries are respected from the original to the prediction. Here, very little magnitude of melt pool depth is seen outside of the plotted contour, indicating that the use of the custom loss function is able to successfully penalize the presence of melt pool outside for the contour. The predicted melt pool topology is then down-sampled to the 5-micron resolution of the simulated ground truth in order to compare the cross-section profiles. From this comparison, close agreement is observed between the ground truth and predicted contours.

Figure 4 shows a similar result for the time evolution of a single melt pool. At $t = 0.165\ ms$, the melt pool is concentrated near the beam and has not reached the steady state behavior, as shown in both simulation and the model prediction. At $t = 0.33\ ms$, the melt pool grows, and this elongation is observed in both the prediction and ground truth cases, with close agreement also observed in the cross-section plot. Finally, near the end of the simulation at $t = 0.495\ ms$, the prediction reflects that the melt pool is fully developed. By training on the time-dependent temperature distribution, the model is able to recreate the transient evolution of the melt pool.

As the keyhole cavity generated during the L-PBF process can become a significant contributor towards the formation of void structures in the finished part, we also investigate the use of this model to predict the surface morphology of the keyhole region. Cunningham et al. (2017) assert that key metrics of the shape of the keyhole, such as the keyhole front and back wall angles, can directly suggest the formation of a pore or void space [8]. Therefore, the constructed network is similarly trained on 64×64 pixel snapshots of the tempera-

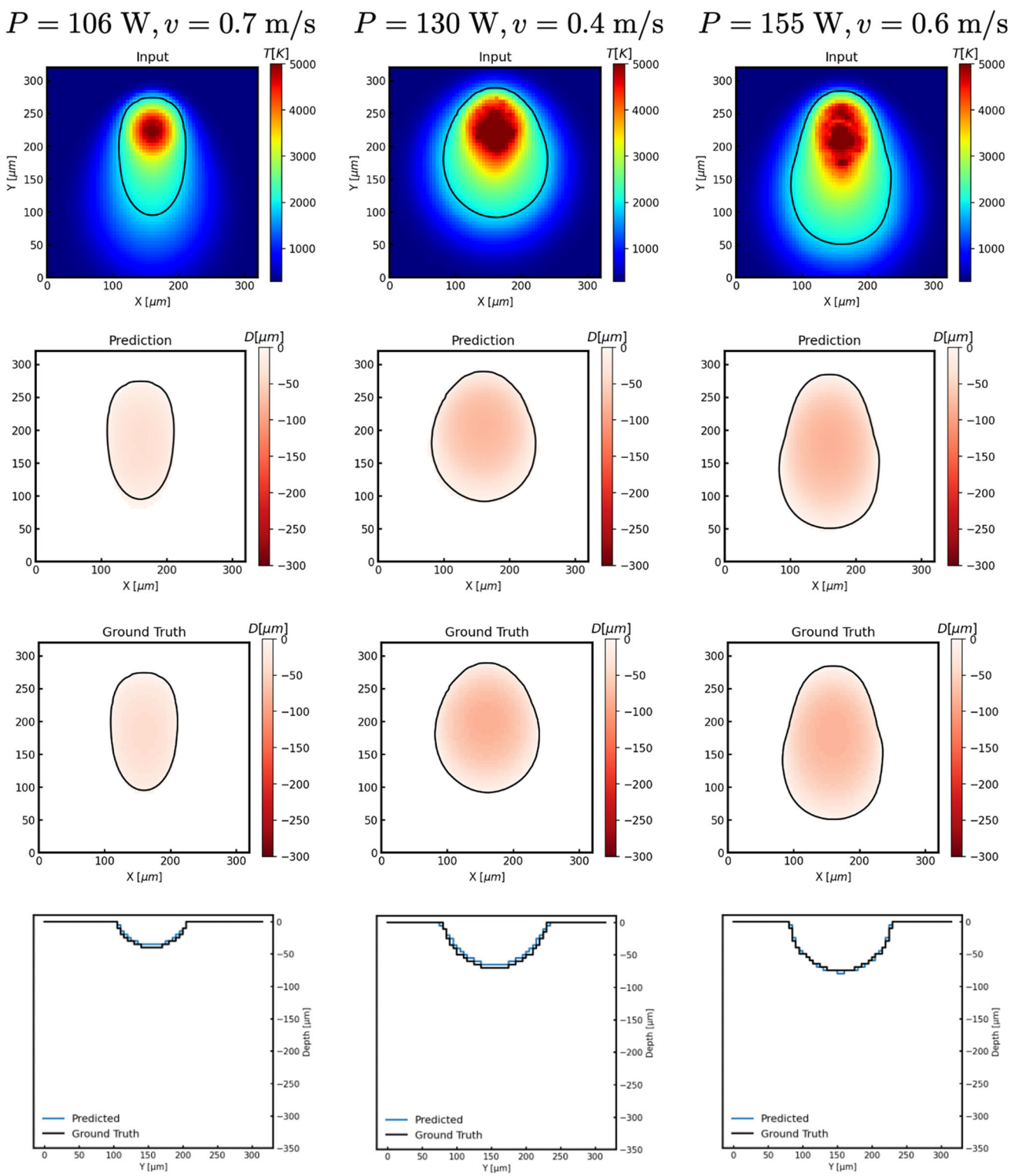


**Fig. 3** The model is used to predict the melt depth at varying process parameter regimes, to analyze performance as the energy density of the temperature input changes. A comparison of the predicted cross section is made with the ground truth cross section, with the prediction downscaled to the same resolution as the mesh used for the ground truth simulation

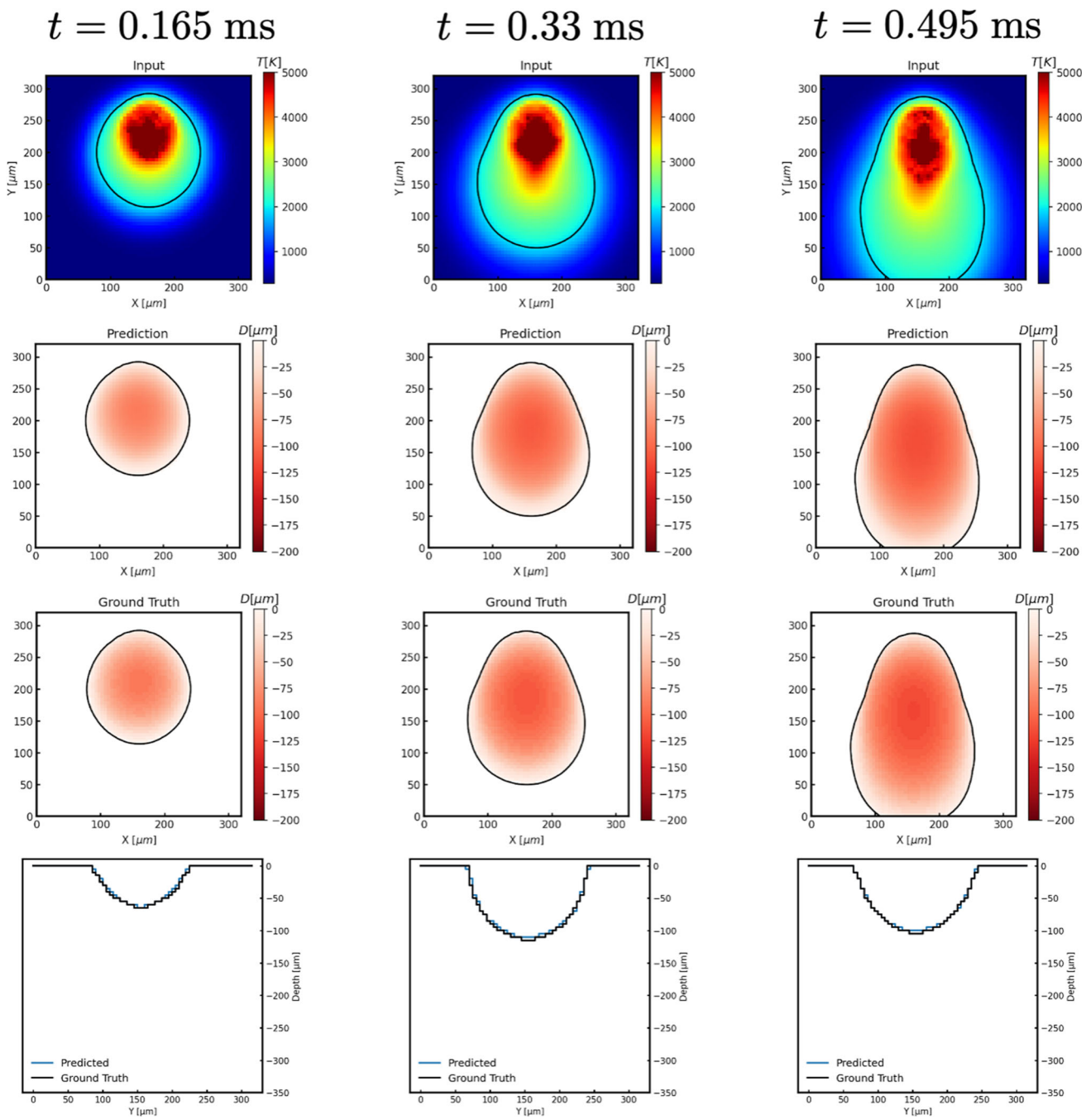


**Fig. 4** The model is used to predict the melt depth at varying timesteps during the melt pool transient evolution. A comparison is made between the predicted cross section and the ground truth cross section

ture distribution with a new target of the keyhole cavity depth contour.

The keyhole cavity topology maps for the ground truth and predicted morphologies are displayed in Fig. 5 to evaluate the accuracy of the model for the keyhole depth prediction task. To enable a visual comparison between the predicted and target images, a contour line is drawn at a threshold depth of $30\mu m$ in the ground truth vapor depression contour map. The vapor depression prediction task is more challenging than the melt depth prediction task, due to the rapidly changing stochastic nature of the keyhole cavity. However, the average width and length is recreated accurately by the model after the training process.

The average error for each combination of laser power and scanning speed found in the dataset is illustrated in Fig. 6a and b for the melt pool depth and keyhole depth prediction tasks,

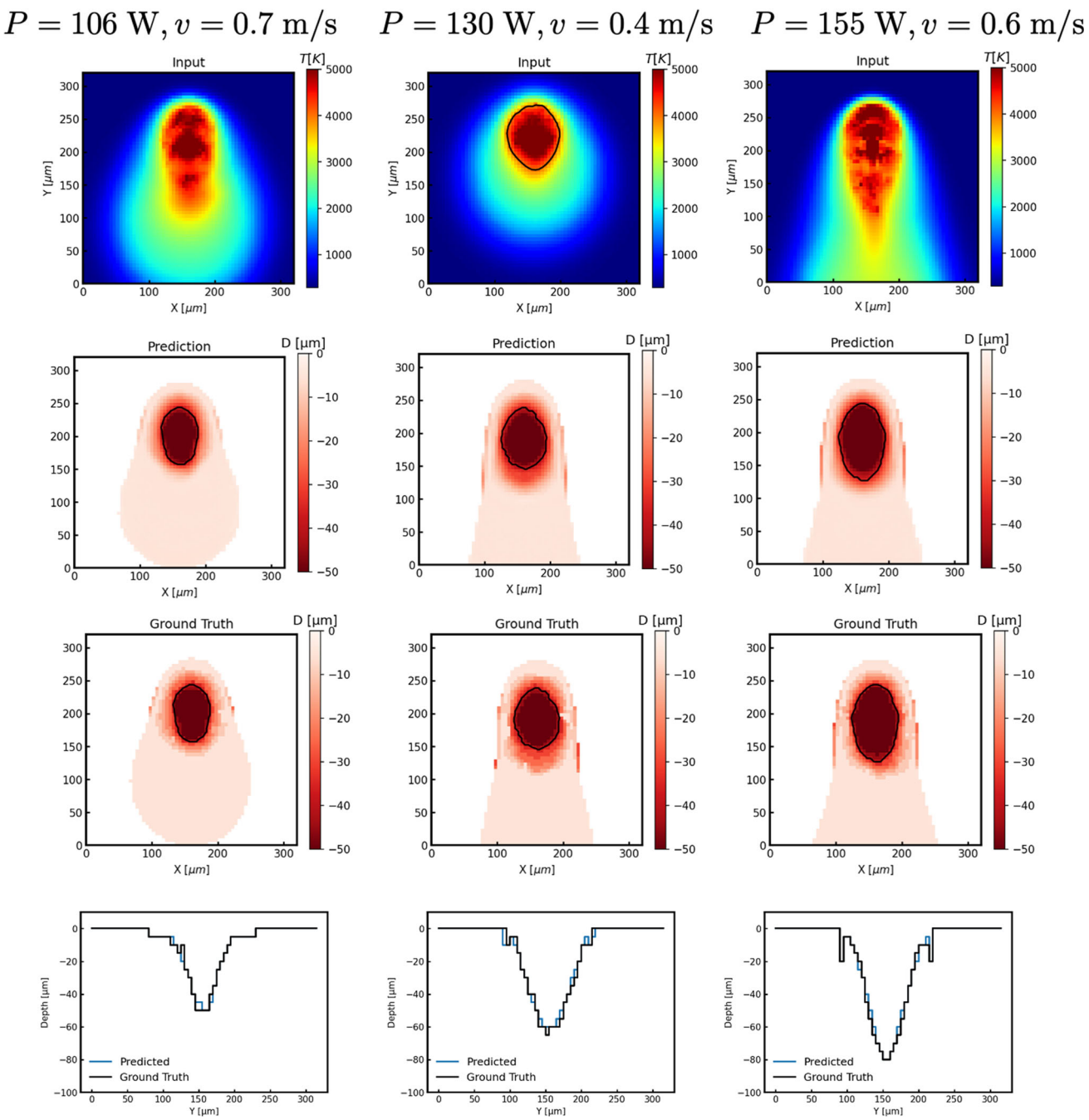


**Fig. 5** The model is used to predict the keyhole cavity depth at varying process parameter regimes, to analyze performance as the energy density of the temperature input changes. A comparison of the predicted cross section is also made with the ground truth cross section, with the prediction downscaled to the same resolution as the mesh used for the ground truth simulation

respectively. The error is maintained within the range of 0–4 $\mu m$ for all combinations, but shows a tendency to increase in high energy density scenarios. This increase in the error associated with the depth prediction task can be attributed to the higher instability of the melt pool at large energy densities. In Fig. 6c and d, the melt pool and keyhole lengths, widths, and depths are extracted and compared to the ground truth predictions. The depth is extracted by finding the maximum depth in the bounding box studied, while the width and length are calculated as the major and minor axes of an ellipse fitted with the same normalized second moments as the melt pool contour [within the bounding box]. The extracted values lie within a correlation $R^2$ of [0.95, 0.996], a promising indicator that the model proposed is generalizable across the

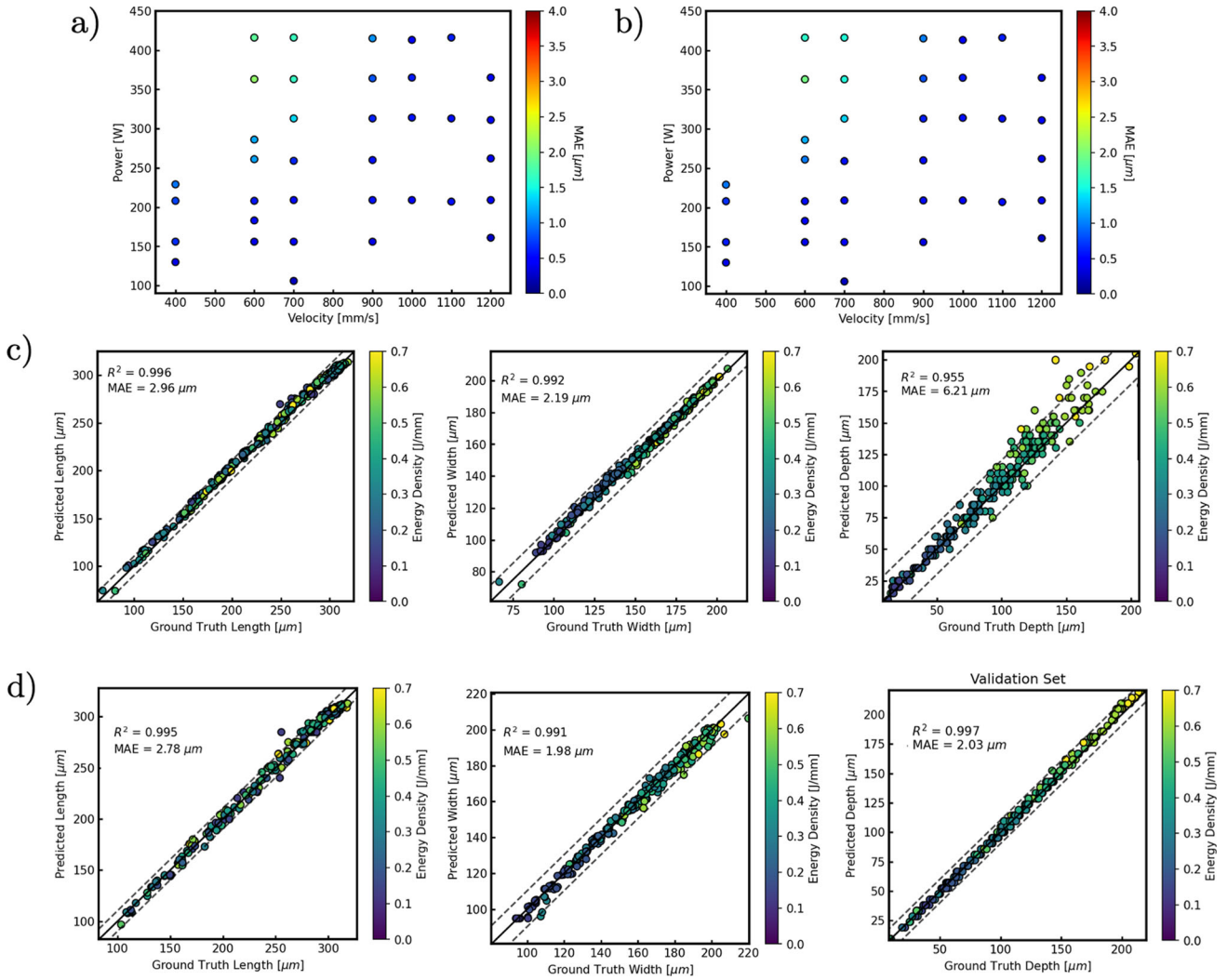


**Fig. 6** **a** The mean absolute error on the vapor cavity prediction task associated with different processing parameters in the dataset. The error is highest in the limit of high power ($P > 400$ W) and low velocity ($V < 800$ mm/s), due to the increased energy density and thus more unstable behavior of the melt pool. **b** The mean absolute error on the depth prediction task, associated with different processing parameters in the dataset. The error is highest in the limit of high power ($P > 400$ W) and low velocity ($V < 800$ mm/s), due to the increased energy density and thus more unstable behavior of the vapor cavity. **c** The keyhole cavity dimensions plotted against the ground truth keyhole cavity dimensions. **d** The melt pool dimensions plotted against the ground truth melt pool dimensions

process regimes studied in this work and does not overfit to a specific area of the process map. However, larger amounts of error are seen in the vapor depression predictions at high energies, which is likely due to the increased instability of the vapor cavity as the melt pool transitions to an unstable keyhole regime.

The 3D topology of the melt pool can be extracted using the predicted melt pool depth and keyhole cavity depth contour maps. From the CNN model, a temperature at the surface input can be converted to a melt depth and vapor depression depth. Following this process, these two contours can be combined on a 3D plot yielding the overall morphology of the free surface of the melt pool. The vapor depression assists in predicting the onset of keyhole behavior, while the melt depth prediction aids in identifying cases where lack of fusion can occur. This is especially useful in scenarios where the volumetric energy density does not necessarily directly translate to the onset of lack-of-fusion effects. Figure 7a demonstrates the 3D prediction for different power-velocity combinations at $t = 0.25$ ms, while Fig. 7b demonstrates the 3D prediction for the same melt pool at different snapshots in time. The size, shape, and orientation of the melt pool are similar across the ground truth and predicted cases, with the variation occurring within the rapidly fluctuating keyhole boundary.

Though this model is created based on a numerical model of the melting dynamics, it can be potentially be extended to experimental scenarios by using temperature data collected

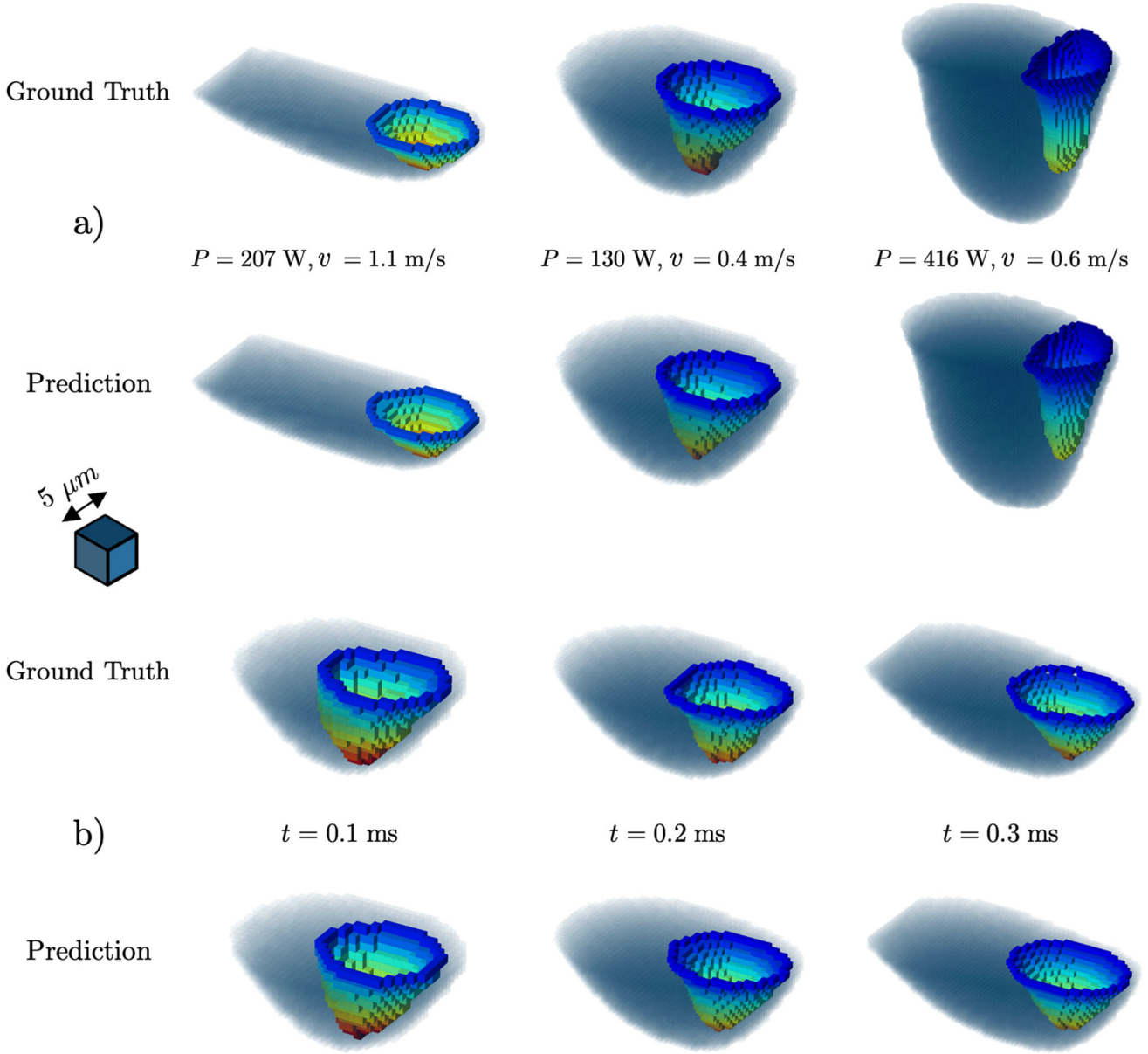


**Fig. 7** 3D reconstructions of the melt pool morphology predicted by the model, compared to the ground truth melt pool. **a** The melt pool ground truth and predictions for different operating conditions at $t = 0.25$ ms. **b** The melt pool ground truth and predictions at different times during the simulations at P = 209 W, V = 700 mm/s

through thermography [37]. These thermal images can be rescaled to match the resolution of the input images used for training and used for inference on a pre-trained model. The challenges inherent in extending to an experimental context include sources of error in terms of the measurements and occlusions preventing the entire melt pool from being imaged. To address these limitations, an ablation study is run to study the effect of changing the degree of augmentation to observe how robust the model is to noise injections. Figure 8a describes the model prediction error on the unseen test dataset as increasing amounts of noise are added to the model. The MAE is much lower on the augmented dataset, as the model is able to produce more generalizable predictions and avoid overfitting. Additionally, an ablation study is carried out in Fig. 8b to determine the optimal configuration of the loss function based on the error on the predicted melt pool surface area. The surface area is calculated as the size of the melt pool footprint viewed from a top-down orientation. The weighting factor, $c$, determines the tendency for the model to prioritize optimizing the melt pool boundaries in relation to the task of optimizing for the correct melt pool temperature distribution.

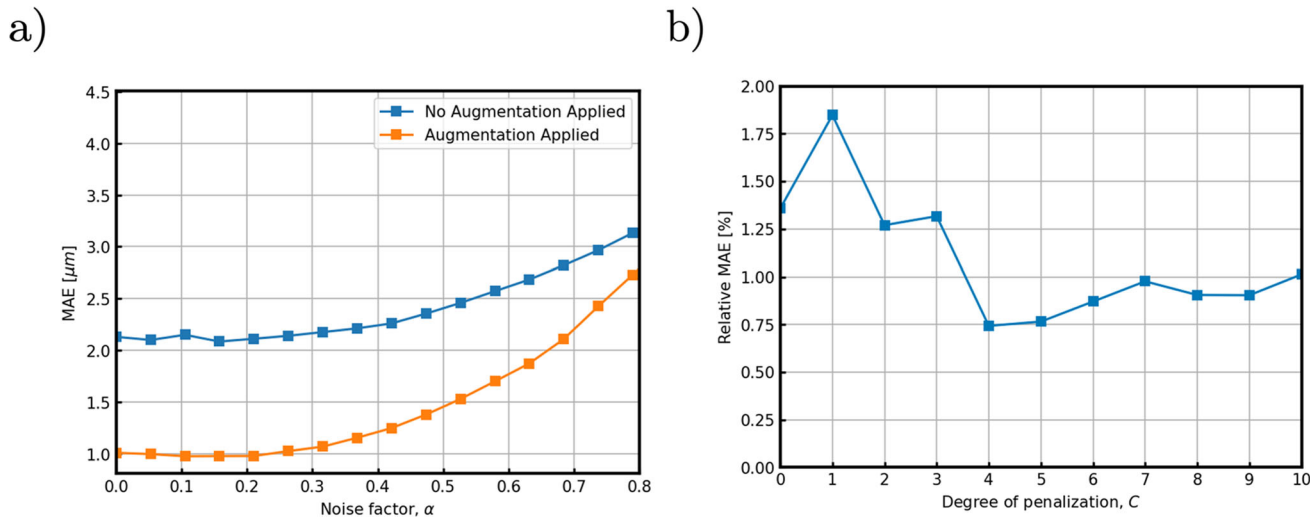


**Fig. 8** **a** The prediction performance of the model trained on augmented data, as the level of noise increases. The prediction error remains constant for increasing amounts of noise added, until very high values of noise are added to the inputs. **b** The prediction performance of the model based on the relative weight, $c$, of the term that enforces the correct melt pool boundary shape. The relative MAE is the normalized error of the predicted melt pool surface area, imaged from a top-down vertical orientation

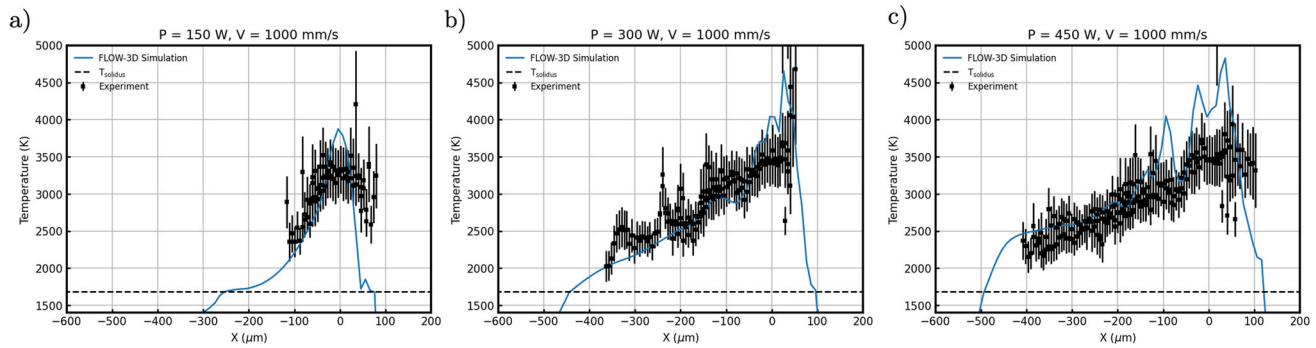


**Fig. 9** A comparison of the observed surface temperatures for single bead SS316L extracted via two-color thermal imaging as described in [38] to the equivalent surface temperatures extracted from $10\mu m$ FLOW-3D simulations. Agreement is observed for large portions of the melt pool. **a** FLOW-3D and experimental measurements taken at $P$ = 150 W, $V$ = 1000 mm/s, **b** FLOW-3D and experimental measurements taken at $P$ = 300 W, $V$ = 1000 mm/s, **c** FLOW-3D and experimental measurements taken at $P$ = 450 W, $V$ = 1000 mm/s. The error bars on the experimental data combine the uncertainty in emissivity and signal, as described in [38]

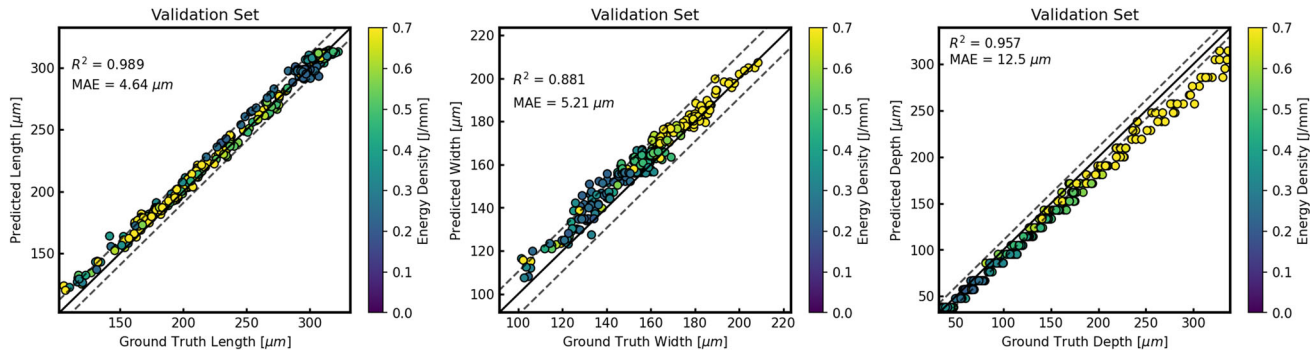


**Fig. 10** The predicted melt pool dimensions within the bounding box compared to the ground truth melt pool dimensions for cases in the SS316L validation set. The ground truth melt pool dimensions are extracted from FLOW-3D simulations at a mesh element resolution of $10\mu m$

**Table 1** The predicted and observed melt pool dimensions at a scan speed of 1 m/s, where experimental thermal images are used as input to the CNN model

| Power (W) | 150 | 300 | 450 |
|---|---|---|---|
| Experimental width ($\mu m$) | $105 \pm 7.98$ | $161 \pm 9.00$ | $181 \pm 4.62$ |
| Predicted width ($\mu m$) | 110 | 150 | 170 |
| Experimental depth ($\mu m$) | $31.0 \pm 3.32$ | $78.9 \pm 4.86$ | $155 \pm 8.58$ |
| Predicted depth ($\mu m$) | 25 | 100 | 134 |

The experimental widths and depths listed are taken from cross-sections of the solidified melt track, and the reported error is two standard deviations [38]

To directly evaluate the generalization capability of the trained model from simulation data to experimental data, we create a dataset of 340 SS316L simulations, using the processing parameters described in the Appendix (Fig. 12). The parameters and implemented physics used in this FLOW-3D simulation are optimized to match experimental thermal measurements, following the process described in Myers and Quirarte et al. [38]. Notably, the empirical absorptivity model described in Sect. 2.1 is replaced with an angle-dependent absorptivity estimate based on Fresnel reflection. Therefore, two parameters are used in this optimization process: the accommodation coefficient and the Fresnel coefficient. The Fresnel coefficient parameterizes the amount of energy absorbed by the melt pool based on the laser angle of incidence, while the accommodation coefficient describes the rate of heat exchange between phases. The accommodation coefficient and the Fresnel coefficient can both significantly alter the relationship between the temperature distribution of the simulations and the dimensions of the melt pool. For instance, both parameters influence the vaporization effects that lead to keyhole formation and convective flows.

The experimental SS316L data used for this comparison is generated by printing no-powder single-bead tracks on a TRUMPF TruPrint 3000 L-PBF machine [38]. A Photron FASTCAM mini-AX200 color camera is used to capture images of the surface of the melt pool at a frame rate of 22,500 frames per second with a pixel size of 5.6 $\mu$m. These images are converted to temperature measurements at each pixel through the two-color method, which reduces the measurement's sensitivity to temperature-dependent emissivity. Specifically, this technique uses the ratio of the red and green channel intensities from the color camera. For a detailed explanation of the experimental methodology, the reader is referred to [38]. The melt pool dimensions are extracted by cross-sectioning, etching, and measuring these single-bead tracks. A comparison between the FLOW-3D data and experimental thermal profiles is reproduced in Fig. 9 for three sets of processing parameters, where the experimental measurements combine images taken at four different camera exposure times (1.05 $\mu$s, 1.99 $\mu$s, 6.67 $\mu$s, and 20 $\mu$s).

We retrain the model with this dataset, decreasing the number of channels at each layer by a factor of four to account for the modified image size. The error metrics following this model training process are shown in Fig. 10.

Finally, we evaluate the generalization capability of this trained model to experimental data. To do so, we provide

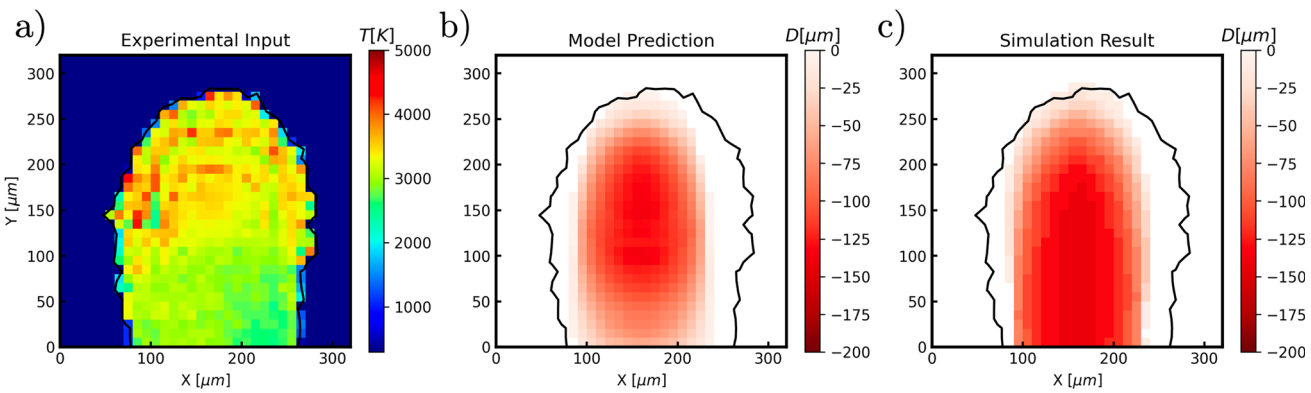


**Fig. 11** **a** A sample experimental two-color thermal image from a single bead SS316L track run at $P = 450$ W, $V = 1000$ mm/s [38]. **b** The predicted melt pool depth contour based on the input thermal image. **c** The melt pool depth contour observed in simulation at $P = 450$ W, $V = 1000$ mm/s, at a mesh element resolution of 10 $\mu m$

the model with experimentally observed two-color thermal images at processing parameters not encountered in the training set [38] and compare the predicted melt pool dimensions to experimental ex-situ measurements of the solidified melt track (Table 1). This is carried out at laser powers 150 W, 300 W, and 450 W, with the scanning speed held constant at 1 m/s. A sample experimental thermal input image is shown alongside the model prediction and corresponding FLOW-3D depth contour map in Fig. 11.

There are several differences between the experimental and simulated data as a direct result of the assumptions of the simulation and the inherent difficulties in experimentally observing the small-scale, high-temperature melt pool behavior. For instance, the vaporized gas can obstruct areas of the observed thermal image, and the assumption of the single-phase interaction between the vapor plume and the melt pool may not fully capture the variability in the possible thermal signatures [38, 39]. Finally, the laser in the experiment impacts the build plate at an angle of approximately 20 degree to accommodate the imaging apparatus [38], which may also influence the agreement between the simulation and experiment.

## 4 Conclusion

In this work, we introduce a convolutional neural network architecture for predicting the 3D structure of the melt pool. Specifically, we decompose this three-dimensional problem into a series of 2D models, one trained to predict the vapor cavity structure beneath the surface and another trained to predict the melt pool depth beneath the surface. After analyzing the performance of the model, the convolutional neural network can successfully predict the melt depth of the laser powder bed. Finally, we demonstrate preliminary generalization to experimental data, where the model is able to generate feasible estimates of the melt pool dimensions based on the thermal images and processing parameters. With these predictions and the ability to have a visualization of the melt pool with just the temperature map and the material properties, defects that occur due to the structure of the melt pool can be caught early to reduce the expenses associated with post-processing or discarding a defective part. However, this work deals only with the instantaneous prediction of the melt pool dynamics, without considering the previous history of the melt pool behavior. Therefore, future work may include extending this model to generalize to cases where the thermal history of the melt pool affects the geometry of the melt pool, including layer remelting and geometrical overhangs. Additionally, this model may also be extended to predict melt pools in an online manner for monitoring in experimental contexts, based on in situ two-color thermal images of the melt pool.

## Appendix. Material and processing parameters

**Table 2** Material parameters used to simulate the Ti-6Al-4V melting process

| Parameter | Value | Units |
|---|---|---|
| Density, $\rho$, 298 K | 4420 | kg/m$^3$ |
| Density, $\rho$, 1923 K | 3920 | kg/m$^3$ |
| Specific heat, $C_v$, 298 K | 546 | J/kg/K |
| Specific heat, $C_v$, 1923 K | 831 | J/kg/K |
| Vapor specific heat, $C_{v,vapor}$ | 600 | J/kg/K |
| Thermal conductivity, $k$, 298 K | 7 | W/m/K |
| Thermal conductivity, $k$, 1923 K | 33.4 | W/m/K |
| Viscosity, $\eta$ | 0.00325 | kg/m/s |
| Surface tension, $\sigma$ | 1.882 | $kg/s^2$ |
| Liquidus temperature, $T_L$ | 1923 | K |
| Solidus temperature, $T_S$ | 1873 | K |
| Fresnel coefficient $\epsilon$ | 0.2 | - |
| Accommodation coefficient, $a$ | 0.15 | - |
| Latent heat of fusion, $\Delta H_f$ | $2.86 \times 10^5$ | J/kg |
| Latent heat of vaporization, $\Delta H_v$ | $6.00 \times 10^4$ | J/kg |

**Table 3** Material parameters used to simulate the SS316L melting process

| Parameter | Value | Units |
|---|---|---|
| Density, $\rho$, 298 K | 7950 | kg/m$^3$ |
| Density, $\rho$, 1923 K | 6765 | kg/m$^3$ |
| Specific heat, $C_v$, 298 K | 470 | J/kg/K |
| Specific heat, $C_v$, 1923 K | 1873 | J/kg/K |
| Vapor specific heat, $C_{v,vapor}$ | 449 | J/kg/K |
| Thermal conductivity, $k$, 298 K | 13.4 | W/m/K |
| Thermal conductivity, $k$, 1923 K | 30.5 | W/m/K |
| Viscosity, $\eta$ | 0.008 | kg/m/s |
| Surface tension, $\sigma$ | 1.882 | $kg/s^2$ |
| Liquidus temperature, $T_L$ | 1723 | K |
| Solidus temperature, $T_S$ | 1658 | K |
| Fresnel coefficient, $\epsilon$ | 0.15 | - |
| Accommodation coefficient, $a$ | 0.25 | - |
| Latent heat of fusion, $\Delta H_f$ | $2.6 \times 10^5$ | J/kg |
| Latent heat of vaporization, $\Delta H_v$ | $7.45 \times 10^6$ | J/kg |

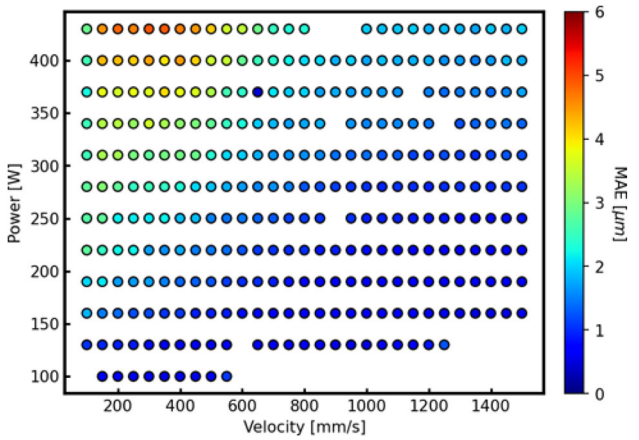


**Fig. 12** The processing parameters generated for the SS316L dataset at a 10 $\mu m$ mesh resolution, colored by the mean absolute error on the melt pool depth prediction task

**Author Contributions** All authors contributed to the project conception and design. Amir Barati Farimani (A.B.F.), Jonathan Malen (J.M.), and Jack Beuth (J.B.) secured project funding and supervised project progress. The first draft of the manuscript was written by Odinakachukwu Francis Ogoke (O.F.O.) and William Lee (W.L.). The simulation data was generated and post-processed by O.F.O. and Alexander Myers (A.M.). The experimental data compilation and analysis was carried out by A.M. The machine learning models were designed by Ning-Yu Kao (N.K.), W.L., and O.F.O. Optimization experiments were carried out by N.K., A.M., W.L., and O.F.O. All authors were involved in the review and editing process.

**Funding** Open Access funding provided by Carnegie Mellon University. Research was sponsored by the Army Research Laboratory and was accomplished under Cooperative Agreement Number W911NF-20-2-0175. The views and conclusions contained in this document are those of the authors and should not be interpreted as representing the official policies, either expressed or implied, of the Army Research Laboratory or the U.S. Government. The U.S. Government is authorized to reproduce and distribute reprints for Government purposes notwithstanding any copyright notation herein.

## Declarations

**Competing interests** The authors declare no competing interests.



## References

1. King WE, Anderson AT, Ferencz RM, Hodge NE, Kamath C, Khairallah SA, Rubenchik AM (2015) Laser powder bed fusion additive manufacturing of metals; physics, computational, and materials challenges. Appl Phys Rev 2(4):041304
2. Sing S, Yeong W (2020) Laser powder bed fusion for metal additive manufacturing: perspectives on recent developments. Virtual Phys Prototyp 15(3):359–370
3. Malekipour E, El-Mounayri H (2018) Common defects and contributing parameters in powder bed fusion am process and their classification for online monitoring and control: a review. Int J Adv Manuf Technol 95(1):527–550
4. Vilardell AM, Fredriksson G, Yadroitsev I, Krakhmalev P (2019) Fracture mechanisms in the as-built and stress-relieved laser powder bed fusion Ti6Al4V ELI alloy. Opt Laser Technol 109:608–615. https://doi.org/10.1016/J.OPTLASTEC.2018.08.042
5. Andreau O, Pessard E, Koutiri I, Penot JD, Dupuy C, Saintier N, Peyre P (2019) A competition between the contour and hatching zones on the high cycle fatigue behaviour of a 316L stainless steel: analyzed using X-ray computed tomography. Mater Sci Eng A 757:146–159. https://doi.org/10.1016/J.MSEA.2019.04.101
6. Gong H, Rafi K, Gu H, Janaki Ram GD, Starr T, Stucker B (2015) Influence of defects on mechanical properties of Ti–6Al–4V components produced by selective laser melting and electron beam melting. Mater Des 86:545–554. https://doi.org/10.1016/J.MATDES.2015.07.147
7. Ogoke OF, Johnson K, Glinsky M, Laursen C, Kramer S, Farimani AB (2022) Deep-learned generators of porosity distributions produced during metal additive manufacturing. Addit Manuf 60:103250
8. Cunningham R, Narra SP, Montgomery C, Beuth J, Rollett A (2017) Synchrotron-based X-ray microtomography characterization of the effect of processing variables on porosity formation in laser power-bed additive manufacturing of Ti-6Al-4V. Jom 69(3):479–484
9. Cao S, Zou Y, Lim S, Wu X (2021) Review of laser powder bed fusion (LPBF) fabricated Ti-6Al-4V: process, post-process treatment, microstructure, and property. Light Adv Manuf 2:20. https://doi.org/10.37188/lam.2021.020
10. Tang M, Pistorius PC, Beuth JL (2017) Prediction of lack-of-fusion porosity for powder bed fusion. Addit Manuf 14:39–48
11. Grasso M, Colosimo BM (2017) Process defects and in situ monitoring methods in metal powder bed fusion: a review. Meas Sci Technol 28(4):044005
12. Bertoli US, Guss G, Wu S, Matthews MJ, Schoenung JM (2017) In-situ characterization of laser-powder interaction and cooling rates through high-speed imaging of powder bed fusion additive manufacturing. Mater Des 135:385–396
13. Kanko JA, Sibley AP, Fraser JM (2016) In situ morphology-based defect detection of selective laser melting through inline coherent imaging. J Mater Process Technol 231:488–500
14. Parab ND, Zhao C, Cunningham R, Escano LI, Fezzaa K, Everhart W, Rollett AD, Chen L, Sun T (2018) Ultrafast X-ray imaging of laser-metal additive manufacturing processes. J Synchrotron Radiat 25(5):1467–1477
15. Hojjatzadeh SMH, Parab N, Yan W, Guo Q, Xiong L, Zhao C, Qu M, Escano L, Xiao X, Fezzaa K, Everhart W, Sun T, Chen L (2019) Pore elimination mechanisms during 3D printing of metals. Nat Commun 10. https://doi.org/10.1038/s41467-019-10973-9
16. Uhlmann E, Krohmer E, Schmeiser F, Schell N, Reimers W (2020) A laser powder bed fusion system for in situ x-ray diffraction with high-energy synchrotron radiation. Rev Sci Instrum 91(7):075104
17. Parab ND, Zhao C, Cunningham R, Escano LI, Gould B, Wolff S, Guo Q, Xiong L, Kantzos C, Pauza J et al (2019) High-speed

synchrotron x-ray imaging of laser powder bed fusion process. Synchrotron Radiat News 32(2):4–8
18. Tyralla D, Seefeld T (2021) Thermal based process monitoring for laser powder bed fusion (LPBF). Adv Mater Res 1161:123–130. https://doi.org/10.4028/www.scientific.net/AMR.1161.123
19. Lane B, Moylan S, Whitenton EP, Ma L (2016) Thermographic measurements of the commercial laser powder bed fusion process at NIST. Rapid Prototyp J 22(5):778–787
20. Fischer FG, Birk N, Rooney L, Jauer L, Schleifenbaum JH (2021) Optical process monitoring in laser powder bed fusion using a recoater-based line camera. Addit Manuf 47:102218. https://doi.org/10.1016/j.addma.2021.102218
21. Montazeri M, Rao P (2017) In-process condition monitoring in laser powder bed fusion (LPBF). In: Solid freeform fabrication 2017: proceedings of the 28th annual international solid freeform fabrication symposium, pp 1264–1278
22. Mohammadi MG, Mahmoud D, Elbestawi M (2021) On the application of machine learning for defect detection in L-PBF additive manufacturing. Opt Laser Technol 143:107338
23. Razvi SS, Feng S, Narayanan A, Lee Y-TT, Witherell P (2019) A review of machine learning applications in additive manufacturing. In: International design engineering technical conferences and computers and information in engineering conference, vol 59179, pp 001–02040. American Society of Mechanical Engineers
24. Akbari P, Ogoke F, Kao N-Y, Meidani K, Yeh C-Y, Lee W, Farimani AB (2022) MeltpoolNet: melt pool characteristic prediction in metal additive manufacturing using machine learning. Addit Manuf 55:102817
25. Gobert C, Reutzel EW, Petrich J, Nassar AR, Phoha S (2018) Application of supervised machine learning for defect detection during metallic powder bed fusion additive manufacturing using high resolution imaging. Addit Manuf 21:517–528
26. Imani F, Chen R, Diewald E, Reutzel E, Yang H (2019) Deep learning of variant geometry in layerwise imaging profiles for additive manufacturing quality control. J Manuf Sci Eng 141(11). https://doi.org/10.1115/1.4044420 https://arxiv.org/abs/https://asmedigitalcollection.asme.org/manufacturingscience/article-pdf/141/11/111001/5431618/manu_141_11_111001.pdf. 111001
27. Lecun Y, Bottou L, Bengio Y, Haffner P (1998) Gradient-based learning applied to document recognition. Proc IEEE 86:2278–2324. https://doi.org/10.1109/5.726791
28. Snow Z, Diehl B, Reutzel EW, Nassar A (2021) Toward in-situ flaw detection in laser powder bed fusion additive manufacturing through layerwise imagery and machine learning. J Manuf Syst 59:12–26. https://doi.org/10.1016/j.jmsy.2021.01.008
29. Flow Science I (2019) FLOW-3D, Version 12.0. Santa Fe, NM . https://www.flow3d.com/
30. Mills KC (2002) Recommended values of thermophysical properties for selected commercial alloys. Woodhead Publishing
31. Spiegel EA, Veronis G (1960) On the Boussinesq approximation for a compressible fluid. Astrophys J, vol 131, p 442. 131:442
32. Hirt CW, Nichols BD (1981) Volume of fluid (VOF) method for the dynamics of free boundaries. J Comput Phys 39(1):201–225
33. Trapp J, Rubenchik AM, Guss G, Matthews MJ (2017) In situ absorptivity measurements of metallic powders during laser powder-bed fusion additive manufacturing. Appl Mater Today 9:341–349
34. Ye J, Khairallah SA, Rubenchik AM, Crumb MF, Guss G, Belak J, Matthews MJ (2019) Energy coupling mechanisms and scaling behavior associated with laser powder bed fusion additive manufacturing. Adv Eng Mater 21(7):1900185
35. Paszke A, Gross S, Massa F, Lerer A, Bradbury J, Chanan G, Killeen T, Lin Z, Gimelshein N, Antiga L, Desmaison A, Kopf A, Yang E, DeVito Z, Raison M, Tejani A, Chilamkurthy S, Steiner B, Fang L, Bai J, Chintala S (2019) Pytorch: an imperative style, high-performance deep learning library. In: Wallach H, Larochelle H, Beygelzimer A, Alché-Buc F, Fox E, Garnett R (eds) Advances in neural information processing systems 32, pp 8024–8035. Curran Associates, Inc
36. Bergstra J, Yamins D, Cox DD (2013) Making a science of model search: hyperparameter optimization in hundreds of dimensions for vision architectures. In: Proceedings of the 30th international conference on international conference on machine learning - Volume 28. ICML'13, pp 115–123. JMLR.org
37. Yavari R, Williams R, Riensche A, Hooper PA, Cole KD, Jacquemetton L, Halliday HS, Rao PK (2021) Thermal modeling in metal additive manufacturing using graph theory – application to laser powder bed fusion of a large volume impeller. Addit Manuf 41:101956. https://doi.org/10.1016/j.addma.2021.101956
38. Myers AJ, Quirarte G, Ogoke OF, Lane BM, Uddin SZ, Barati Farimani A, Beuth J, Malen J (2023) High-resolution melt pool thermal imaging for metals additive manufacturing using the two-color method with a single color camera. Additive Manuf 73:103663. https://doi.org/10.1016/j.addma.2023.103663
39. Chen H, Yan W (2020) Spattering and denudation in laser powder bed fusion process: multiphase flow modelling. Acta Mater 196:154–167

## Authors and Affiliations

**Francis Ogoke[1] · William Lee[1] · Ning-Yu Kao[2] · Alexander Myers[1] · Jack Beuth[1] · Jonathan Malen[1] · Amir Barati Farimani[1,2,3]**

Francis Ogoke
oogoke@andrew.cmu.edu

William Lee
wlee4@gmail.com

Ning-Yu Kao
kaoningyu@gmail.com

Alexander Myers
amyers2@andrew.cmu.edu

Jack Beuth
beuth@andrew.cmu.edu

Jonathan Malen
jonmalen@andrew.cmu.edu

1 Mechanical Engineering, Carnegie Mellon University, 5000 Forbes Avenue, Pittsburgh, PA 15213, USA

2 Chemical Engineering, Carnegie Mellon University, 5000 Forbes Avenue, Pittsburgh, PA 15213, USA

3 Machine Learning, Carnegie Mellon University, 5000 Forbes Avenue, Pittsburgh, PA 15213, USA